1. Introduction

There is an increasing demand for the availability of high resolution environmental topographic datasets (Mancini et al., 2013). Topographic data such as Digital Surface Models (DSMs) offer a valuable insight into the landscape, morphology and elevation structure of an environment (Hutchinson and Gallant, 2000). Progression in topographic modelling has resulted in significant advances in the understanding of geomorphological processes, landform morphometry and morphodynamics. DSMs help achieve understanding by allowing the extraction of crucial information such as slope, aspect, curvature, and the calculation of 3-dimensional metrics such as volume (Bonumá et al., 2014; Ouédraogo et al., 2014). DSMs provide key boundary conditions for numerical modelling of environmental systems. Furthermore, with increasing uncertainty in future environmental changes (IPCC, 2007), having a firm understanding of local environmental morphology and processes has never been more important (Gonçalves and Henriques, 2015).

Aerial photogrammetry and stereo-mapping for topographic applications has been undertaken using aerial photography since the 1930s (Colomina and Molina, 2014). Typically comprising multiple overlapping images taken from a moving camera, aero-triangulation is performed to recover the elevation of the target surface above an established datum. Since the 1990s, topographic mapping on a national scale has been largely superseded by laser-based techniques such as aerial Light Detection and Ranging (Lidar), and space-based Radio Detection And Ranging (RADAR). For smaller areas (i.e. 10s – 100s m) Terrestrial Laser Scanners (TLS) are increasingly used, offering millimetre range precision; in-combination with instruments such as differential GPS (dGPS) and Total Stations, they can prove to be very effective for detecting and measuring morphology and morphological change (Rosser et

al., 2005; Bangen et al., 2014). The expense of airborne techniques, the lack of control over timing of national Lidar-mapping programmes, and possibly the accessibility limitations of some of these approaches has led some scientists to explore the potential of Unmanned Aerial Systems (UASs) for the acquisition of high resolution imagery and elevation mapping through low-altitude aerial photogrammetry (Boon et al., 2016; Clapuyt et al., 2016; Fonstad et al., 2013; Mancini et al., 2013; Ouédraogo et al., 2014).

Developments in UAS photogrammetry align with two fundamental drivers. First, advances in UAS technology and the quality of low-cost consumer grade cameras have allowed researchers with a very small budget to collect high quality aerial imagery. Second, significant research in the field of Computer Vision (CV) has resulted in the development of many novel processing techniques, such as Structure from Motion (SfM). These techniques have improved the performance, efficiency and availability of software for the construction of 3D models of landforms and landscapes (Smith et al., 2016). Much of the processing software is available open-source, and allows for the production of high accuracy topographic models with limited knowledge in photogrammetry (James and Robson, 2012; Westoby et al., 2012).

Critical to topographic modelling is uncertainty quantification. This is especially relevant when calculating and monitoring morphological change where confidence of observed changes is dependent on the appropriate assessment of photogrammetric errors. To account for this, conventional methods such as specifying a minimum level of detection threshold ($_{min}$LOD) are used (Fuller et al., 2003; Milan et al., 2011), where change smaller than the $_{min}$LOD is regarded as noise. Thresholds tend to be calculated so that they represent a 95% confidence level (James et al., 2017a). Calculation of a threshold value can also be

undertaken manually if both the instrument error and expected change rates are known (Lague et al., 2013). However, this induces the potential risk of discarding real geomorphological change. In studies where the expected rate of change is similar to the instrument error, a declining weighting function (Lane et al., 2003) can also be used to avoid discarding potential real change. More robust and sophisticated methods for distinguishing between noise and real change utilise DSM differencing and standard spatially uniform analysis (Wheaton et al., 2010) as well as the utilisation of precision maps (James et al., 2017a). Without the inclusion of accurate error estimation and noise detection system, robust measurement of elevation change in UAS-derived topographic maps is not possible. Calculation of the Root Mean Square Error (RMSE) between a derived model and dGPS-measured ground check points (not included within the bundle adjustment model optimisation) proves useful for quantifying the accuracy achieved within the model (e.g. Lucieer et al., 2014). Accuracies of UAS-derived DSMs vary with flight specifications (i.e. altitude), as well as individual literature examples, such as those discussed within this paper. In general, RMSE in the vertical axis is expected within the range 0.05-5 m (Ouédraogo et al., 2014; Smith et al., 2016; O'Connor et al., 2017). However, there is little consistency, and in some cases an absence (e.g. Boon et al., 2016; Casella et al., 2016) of an examination of the camera calibration methods. Whilst a number of photogrammetry-focused studies document specifically the mitigation of errors in UAS-derived topographic modelling (Wackrow and Chandler, 2011; James and Robson, 2014; Girod et al., 2017), there is limited evidence of the incorporation of key methods such as inclusion of oblique imagery or pre-calibration within the broader geoscience literature. We therefore intend to address this issue by exploring preprocessing techniques when only single-scale nadir imagery (the favoured approach for environmental mapping) is available. This is particularly useful for surveys where oblique imagery or multi-scale nadir (i.e. overlapping nadir images acquired from

multiple altitudes) is not possible (possibly due to timing or battery constraints), or for existing datasets where oblique imagery is absent.

Perhaps the most significant systematic error associated with UAS-derived DSMs is caused by poor calibration of the camera model (James and Robson, 2014) largely associated with radial distortion, a quadratic form of optical aberration, that increases in magnitude with distance from the optical centre (Luhmann, 2013). Calibration of radial distortion has been studied extensively by the photogrammetry community, and as a standard is quantified using Brown's Distortion Model (Fryer and Brown, 1986). Unless camera models account for accurate representations of distortion, broad-scale deformations ('doming' or 'bowling') will occur, resulting in a tendency for significant increase in systematic distribution of vertical error (Javernick et al., 2014; James and Robson, 2014). These errors are most evident on flatter, structure-limited surfaces. This is usually accredited to a lack of strong geometric features within the scene which are important for the self-calibration of the camera model causing systematic distortion (Wackrow and Chandler, 2011), as well as making the deformations visually more obvious. Moreover, it is possible that topographic heterogeneity in landscape applications has permitted the geoscience community to simply overlook such errors.

In this paper, we focus on the demonstration of intrinsic camera distortion effects in SfM analyses undertaken within a low-elevation, low-topographic variance, marginal coastal salt marsh. Saltmarshes occupy the upper part of the vertical tidal zone; they are low-lying and relatively featureless at the broader scale, but comprise distinct microtopography associated with creek systems at the local scale. Accurate topographic mapping of these types of environment is important for monitoring, management and conservation, and essential for

environmental modelling where results are sensitive to errors in the representation of morphology (e.g. hydrodynamic modelling; Cea and French, 2012). There are relatively few studies of the application of UAS-SfM to these topographically-limited terrains. Here, we follow a multi-parameter, multi-software approach to evaluate errors and uncertainties in the development of UAS-derived DSMs. The key objectives are to i) illustrate how varying preprocessing techniques and procedural approaches can be used to limit the effect of systematic radial distortion and ii) propose a concise and robust workflow for the construction of UAS-derived topographic models in even the most topographically-limited (low amplitude, linear) environments. These approaches for distortion mitigation are applied in popular open-source and commercial software.

2. Methodology

2.1 Study area

Salt marshes are found along most of the high water margin of the Deben estuary in Suffolk, eastern UK (Figure 1), and in many cases they are backed by a seawall protecting low-lying grazing or arable land. Salt marsh is an important habitat and natural flood and erosion defence within the Deben estuary, and there is significant interest locally in conservation and positive management approaches to sustain the integrity of the marshes, and concern that rising sea level, increased storm surges, extreme weather events, and boat traffic are contributing to erosion (Reid, 2013). Salt marsh within the Deben estuary occupies elevations around 2-2.5 m Ordnance Datum (OD), (i.e. between mean high water neaps and highest tide level), which is up to 2 m higher than the surrounding land that it protects (Environment Agency, 2011).

Figure 1. Location of the saltmarsh at Bawdsey in the lower reaches of the Deben estuary, east Suffolk, UK. The region of interest is delineated in red on a UAS-derived orthophoto mosaic acquired during the field survey, with the location of dGPS-surveyed control points and transect line for comparison with Lidar data, provided.

2.2 Data collection

The study area was surveyed using a DJI Phantom 4 Pro+. The UAS has a built-in RGB camera; equipped with a Sony Exmor R 1-inch sensor capable of 20MP images. The camera has an advertised focal length of 8 mm and also benefits from a global shutter that eliminates rolling shutter distortion. Salt marsh and tidal flats covering 13 ha were surveyed in a single flight where only single-scale nadir images were captured. Image overlap was set to 80%

front overlap and 60% side overlap to ensure that every point on the ground along the flight path is seen by at least 5 cameras, thereby permitting multi-stereopsis (Furukawa and Ponce, 2010). Although smaller overlaps are used within the literature (i.e. James and Robson, 2014), it is generally considered where possible at least an 80/60 overlap should be sought (O'Connor et al., 2017). Flying at c. 120 m elevation, the on-board UAS camera delivered a 2.2 cm per pixel resolution, requiring 135 images to cover the study area.

A total of 11 ground control points (CtrlPts) comprising 40x40 cm orange plastic markers were measured using a differential GPS system (Leica 1200 base station with GS15 rover) to georeference the point cloud. Leica dGPS systems provide a measure of horizontal and vertical Coordinate Quality (CQ) for each reading, and the average CQ for the CtrlPts was 0.77 cm in x,y position and 1.11 cm for height (Z). This resulted in a combined average 3D CQ of 1.36 cm with a maximum single-point 3D CQ of 2.24 cm. This maximum value was used as the CtrlPt accuracy in both Photoscan and Micmac. GPS-derived camera locations for each image were also used as control observations for the bundle adjustment. An accuracy value of 10m was set which is the manufacturer recommended value for standard GPS devices. Tie point accuracy was set to 1 pixel for both Photoscan and Micmac. This is set lower than the Photoscan default of 4 pixels as the default value has been demonstrated to be too conservative in other similar processing scenarios. Therefore, a lower value is adviced (James and Robson, 2017). The camera location and tie point accuracy value was consistent for all processing scenarios in both Photoscan and Micmac. In addition to CtrlPts, a total of 259 ground check points (ChkPts) were surveyed evenly across the study area using the dGPS device. These were used to quantify the error in constructed DSMs. Check points (ChkPts) were also collected systematically between two CtrlPts to determine if errors

significantly increase with distance from CtrlPts. All dGPS data were referenced spatially to British National Grid, and vertically to Ordance Datum (OD).

2.3 SfM workflow

There are many photogrammetric software packages capable of performing SfM (Fonstad et al., 2013). Advances in these include improvements in the self-calibration of low-cost (non-metric) consumer grade cameras during the bundle adjustment, which means that users with low-cost cameras and/or little knowledge of photogrammetry can undertake SfM with relative ease (Fraser, 2013). However, within a geoscience application, a lack of appreciation of the errors and their sources can make the data, for many applications, unusable (Wheaton, 2009). Commercial software (e.g. Agisoft Photoscan, 123D Catch, Pix4D, Drone Deploy) here are assumed to process data using SfM algorithms, packaged within intuitive and user-friendly graphical user interfaces. A typical workflow starts with determining matching (feature) points across images by utilising the Scale Invariant Feature Transform (SIFT) or a similar algorithm (Lowe, 2004). The next stage incrementally computes the initial pose of camera pairs. Once an initial estimation of the camera pose is determined, this process is repeated until all cameras (where possible) are aligned to the reconstruction. Camera poses and feature points coordinates are then optimised using the bundle adjustment. Dense matching is then derived from implementations of multi-view stereo (MVS) algorithms. Typical methods employed are based on semi-global matching (Hirschmuller, 2005), patch-based (Furukawa and Ponce, 2010), or optimal flow (Pierrot-Deseilligny and Paparoditis, 2006) algorithms.

It is arguable that commercial software is over-automated and the processing is undertaken within a 'black-box' context (Fraser, 2013) where important operations such as camera calibration and absolute orientation transformations become hidden (Wackrow and Chandler, 2011). In contrast, open-source software (i.e. OpenSfM, VisualSfM, Micmac, Bundler) have similar functionality, but usually lack an intuitive user interface, and, in some cases, are run completely from command line interfaces. The command line approach often allows for greater control at every stage of processing; however, it usually requires more experience and user knowledge. Two packages were utilised here, the commercial Agisoft® Photoscan (version 1.3.0) and open source MicmacIGN (Rupnik et al., 2017). DSMs were constructed in each, following a set of processing choices. For both packages, DSMs were constructed with a combination of pre- and self-calibrated camera models using UAS_{GPS} and CtrlPts, achieved through eight processing scenarios (Table 1).

Table 1. List of processing scenarios carried out for quantitative analysis. UAS_{GPS} scenario is where no CtrlPts are used and georeferencing information comes from the on-board GPS that provides camera positions. $dGPS_{ctrl}$ scenario is when dGPS CtrlPts are used as observations in the bundle adjustment, in addition to the on-board GPS for camera positions.

Scenario	Photoscan	Micmac
1	UAS_{GPS}: Self-Calibration	UAS_{GPS}: Three Level Self-calibration
2	UAS_{GPS}: Pre-Calibration	UAS_{GPS}: Pre-Calibration
3	$dGPS_{ctrl}$: Self-calibration	$dGPS_{ctrl}$: Three Level Self-calibration
4	$dGPS_{ctrl}$: Pre-Calibration	$dGPS_{ctrl}$: Pre-Calibration

UAS_{GPS}: UAS onboard GPS
$dGPS_{ctrl}$: Control points measured with dGPS

A well-practised assumption for all photogrammetry problems is that the lens used for data acquisition will inherently result in some form of image distortion. This is due in part to optical components of the lens system not transmitting light in a perfectly linear manner (Luhmann et al., 2013). Whilst the severity of distortion will differ between cameras, it is still

essential to determine a calibration model to rectify the image of such distortions. In general, there are two common approaches to determine the camera model in SfM scenarios. The first is pre-calibration. This is where the user determines the intrinsic geometry and distortion model of the camera before the bundle adjustment in the SfM workflow. In some cases, for high-end cameras this can be done professionally by the camera manufacturer as it is often assumed that the intrinsic geometry of a camera is constant, and therefore will not change after construction, as long as no serious physical impact occurs. A more common method of pre-calibration is a user calibration where a 2D planar pattern is observed from multiple angles. This method was made popular by Triggs (1998) and Zhang (2000). Here, we adopted this technique, capturing images of a black and white checkboard from 34 different angles as in accordance with Chari and Veeraraghavan (2014). The intrinsic and distortion model parameters, radial, tangential, principal point co-ordinates and focal length, were then computed using the 'Camera Calibrator' toolbox available in Matlab. To ensure internal stability of the camera during calibration and data acquisition, camera settings were set to those used during the flights. This is important as both focal length and aperture can have significant influence on distortion and the calibration parameters computed (Läbe and Förstner, 2004).

The second approach is referred to as a self-calibration. This is where camera calibration parameters are determined during the bundle adjustment. One advantage of self-calibration for UAS photogrammetry is that the parameters are determined at the scale of data acquisition. As pre-calibration is determined from images at close-range (i.e. < 10 m), a small error as a result of poor calibration in close-range will be propagated as distance between the camera and feature is scaled up for applied UAS surveys. When surveying flat topographies, if oblique imagery is not included in the bundle adjustment, the self-calibration is mostly

derived from changes in two dimensions as opposed to three for effective parameter optimisation. It is useful to compare this to a pre-calibration of a 2D planar checkboard where the displacement of the board is only in the x and y orientation. Self-calibration usually achieves the goal of solving the parameters of the Brown distortion model (Fryer and Brown, 1986). To solve a full Brown distortion model, a total of 10 parameters must be computed (Fraser, 2013). However, rigorous results are only possible when the image networks are highly redundant with strong convergent geometry. Consequently, in surveys where only single-scale nadir imagery is used, solving Brown's distortion model accurately for all parameters during self-calibration is unlikely. It should be noted that recent studies (e.g. Carbonneau and Dietrich, 2017; James and Robson, 2014) have demonstrated further processing can be used to refine the calibration model parameter values but these approaches are not implemented in any SfM software packages.

Micmac differs to Photoscan in the fact that the calibration model can include a range of different distortion models (see Rupnik et al, 2017). Furthermore, the user can stack a non-radial 7^{th}-order polynomial onto the model to allow for more model parameters. Photoscan estimates distortions using Brown's distortion model; Micmac offers more flexibility in the calibration model and therefore can allow for a more project-specific calibration model to be adopted, benefitting from evolving experience as well as from trial and error. Tournadre et al. (2015) compared the models using UAS data over a linear terrain and concluded that the Four model with a non-radial 7^{th}-order polynomial correction stacked on top (F15P7) gave the best results. The 'Four' self-calibration model is based on the work of Tang et al. (2012) and is designed specifically for aerial camera calibration. It models distortion using Fourier series as the mathematical basis for the self-calibration, and adding a 7^{th}-oder polynomial introduces increased degrees of freedom with respect to the Brown distortion model, creating a more

complex calibration model. Self-calibration within Micmac is performed in three stages to avoid over parameterising the model (Tourandre et al., 2015). The first stage extracts the focal length and calculates the first three radial coefficients on a small subset of data (10 images). This is then applied to all images and the calibration parameters are optimised. The third stage adds a 7th-order polynomial model correction to the coefficients and returns the completed calibrated coefficients in .xml format (Tang et al., 2012). This stage is computed separately because estimating so many parameters at once would likely produce poor results (Tournadre et al., 2015; Rupnik et al., 2017). It is preferable to estimate first on a small sub-set of images with fewer parameters and then estimate the high degree polynomial as a modification of the initial model estimation (Rupnik et al., 2017). Here, the 15x2 refers to a polynomial radial distortion model of 14 parameters for degree 2 general polynoms ($r_3p^3 + \cdots + r_{15}p^{15}$). After the 7-polynomial correction there are a total of 66 parameters. It should be noted that whilst this seems to contradict findings from Wolf et al. (2014), who found that the Brown calibration model gets over parameterised when handling image sets where there is limited geometry, this is not the case here; within Micmac the Four self-calibration yielded the lowest ChkPt RMSE in the Z-axis when compared to other common calibration models (Fraser basic/extended, radial basic/extended) on image-sets with purely aerial single-scale nadir imagery.

Furthermore, we found the lowest RMSE for control and ChkPts in Photoscan (prior to dense matching) was derived when four parameters of radial distortion were used in the distortion model. This subsequently allowed Photoscan and Micmac's distortion coefficients to be compared side-by-side (Table 2). Whilst a thorough investigation into over-parameterisation is not present here, such a study could offer a valuable insight when using calibration models where the full number of parameters is not required (i.e. Brown distortion model).

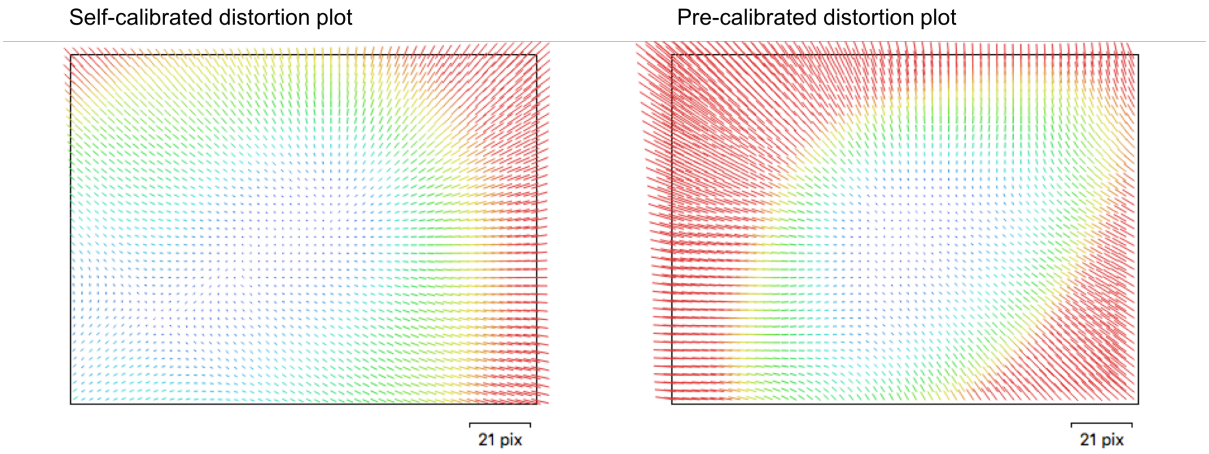

Figure 2. Distortion plot of the built-in UAS camera for self (left) and pre-calibrated (right) calibration models processed in Photoscan where CtrlPts were used. Pre-calibration appears to model a greater magnitude of distortion. The most notable difference is the increased severity in distortion correction for the pre-calibrated model. This correction is responsible for the decreased 'doming' in the reconstructions using the pre-calibrated model. The scale is provided for the correction vector length only.

Photoscan has just three main functions to produce a dense point cloud. First, 'Align Images' is used to carry out feature detection, matching and sparse point cloud generation. If CtrlPts are available, the data can be supplied and the 'Optimize Camera' function is then used to re-adjust the sparse point cloud with respect to the CtrlPts. The function will also perform a bundle adjustment using the CtrlPts as weighted observations. This in turn refines the intrinsic and extrinsic properties for each camera. This is important in reconstructions where there is poorly convergent geometry (e.g. linear topographic surveys with single-scale nadir-only imagery) where accurate camera calibration is not expected from image data alone. Finally, the 'Build Dense Cloud' function can be run. Micmac requires slightly more functions and involves a more fragmented, less autonomous approach to derive a dense point cloud (Figure 3). First, 'Tapioca' is used for feature detection and matching. 'Tapas' is then

called to carry out the bundle adjustment and compute distortion parameters. One of the main parameters for the 'Tapas' function is selection of camera model ('Four' is used in this instance). 'GCP/CentreBascule' is then used to transform the sparse point cloud from an arbitrary co-ordinate system into a geographical one. This can be achieved by using either the GNSS values available in the EXIF metadata, or using an xml file outlining image pixel and geographical coordinates of CtrlPts (created using the 'SaisieAppuis' GUI). If CtrlPts are used, the 'Capari' tools pararmeter 'All Free' parameter should be set, freeing the camera calibration parameters. This is turn allows the CtrlPts to be used as observations in the bundle adjustment in a similar manner to Photoscans 'Optimize Camera's' function. The dense depth map can then be computed using the 'Malt' command. Finally 'Nuage2Ply' can be used to convert the dense depth map into '.ply' format for export into other software. A complete list of commands used is provided in the Appendix.

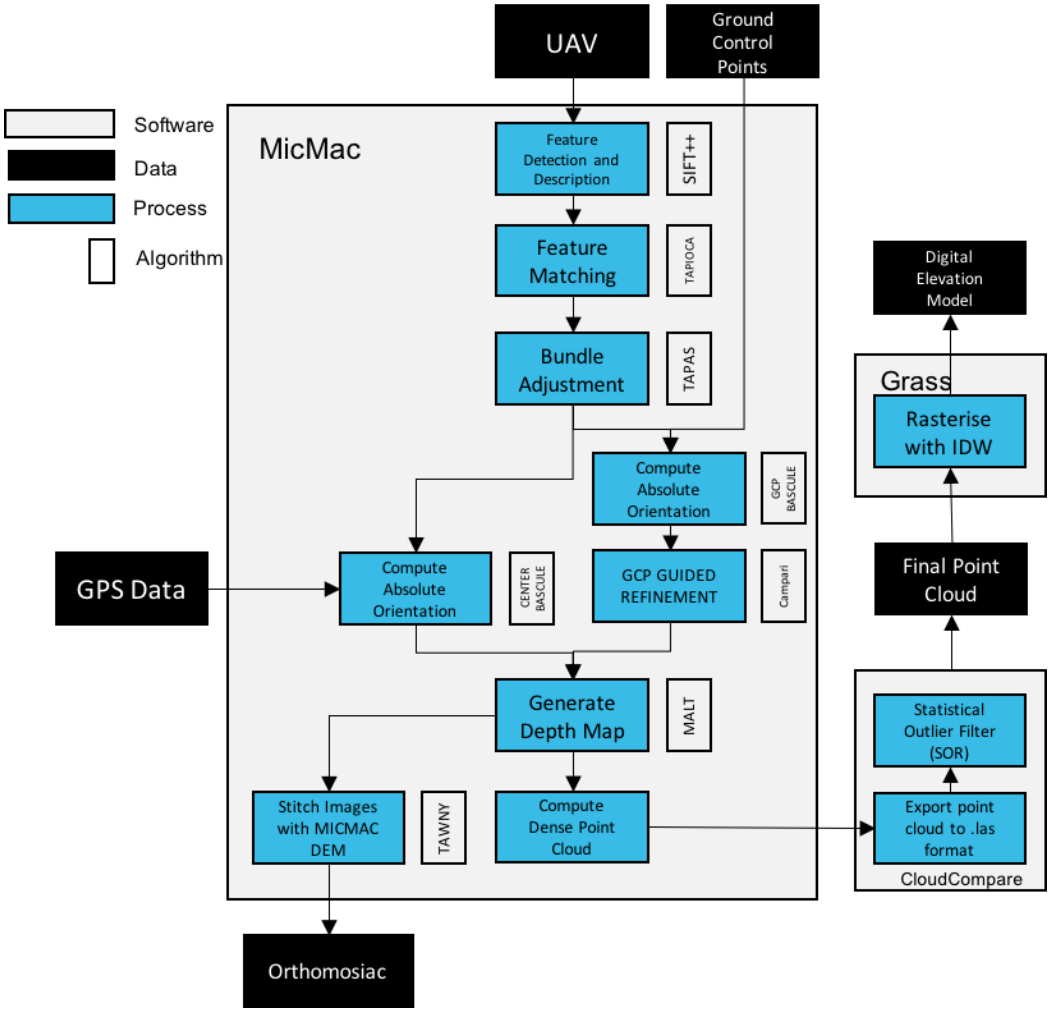

Figure 3. Micmac workflow for UAS-DSM generation. Photoscan achieves the dense point cloud using the standard pre-defined workflow. The proceeding steps are than carried out in the same manner as Micmac.

2.4 Validation

Validation was undertaken by assessing the difference between DSMs constructed from the point cloud and dGPS-surveyed check points (ChkPts). Photoscan and Micmac compute point clouds and DSMs in fundamentally different ways. Micmac computes a regular gridded elevation map where each grid tile is given an elevation value as well as an orientation based on the estimated tile normal direction. The dense matching algorithm used here (Malt Ortho)

therefore creates a dense raster map prior to deriving a 3D point cloud. This means the DSM construction naturally comes before the dense-point cloud generation in the work-flow. To compute the dense point cloud, each tile is sampled and a point is created at the centre of the tile taking the elevation as well as a RGB value (using the Nuage2Ply function). This process explains why the Micmac point cloud is uniformaly distributed. Photoscan, however, has a differing approach and generates a dense 3D point cloud directly by merging image depth maps. As the built-in Photoscan DEM generation tool uses an Inverse Distance Weighting (IDW) algorithm we decided here to use the same with Grass GIS. Each DSM was computed at a resolution of 4 cm/px, and geo-referenced to British National Grid (ESPG: 27700) coordinate system.

Whilst elevation (Z) accuracy can be easily extracted from the produced DSM in a GIS, this is not possible with horizontal (XY) accuracy. To compute the horizontal accuracy, ChkPts acquired on the corners of features easily detectable in the DSM were utilised. We achieved this by measuring the distance between the recorded dGPS location and the observed location of the feature in the DSM.

In addition to comparison with dGPS-surveyed ChkPts, recent Lidar DSM data (sourced from the Environment Agency, provided at 1 m resolution, surveyed in 2017) was compared with the UAS-derived DSMs. The Lidar data was used to create a DSM of Difference (DoD) for each UAS-derived DSM (Brasington et al., 2003) and also to offer a comparative analysis of topography along a 400 m transect extending across the region of interest. Although there is a small time lag between Lidar and UAS surveys (April and June respectively), it is unlikely to have resulted in significant changes in surface level because salt marsh and mudflat environments have small-scale sedimentation rates, and much of the vegetation structure is

retained year-round. In combination with the dGPS survey points, the Lidar data provides a spatially-coherent resource with which to evaluate the complete DSM against.

Analysis of the onboard GPS data revealed the altitude readings on the UAS were grossly incorrect. As these readings get used for initial estimations of each cameras exterior orientation, large errors can cause erroneous bundle adjustment results, and therefore an overall less accurate reconstruction. It is known that GPS is unreliable for obtaining altitude (e.g. +/- 15 m; Blewitt, 2016); however, errors observed were in the region of +/- 100 m. These errors were not systematic and could vary by up to 50 m between successive images. The UAS uses the relative difference in air pressure as read by an on-board barometer to compute relative altitude from its take-off position. Whilst this is primarily used for automated flying, the measurement is recorded within the image metadata. The take-off height was recorded with the dGPS and this value added onto the barometer relative height reading. This gave a much more stable and accurate altitude reading. The UAS_{GPS} data was subsequently replaced with the new measurement which offered much more appropriate camera position estimates for the bundle adjustment.

3. Results

Eight DSMs were successfully computed from UAS-delivered point clouds and compared to the reference Lidar dataset using GRASS7-QGIS (Figure 4 and Figure 5). As the study is in reference to nadir photogrammetry all results were generated from nadir (+/- 2˚) imagery. The DSMs all capture the main features and structures of the site, but there are clear differences in the outputs, and these are often emphasised in the centre or the periphery of the DSM. Strong gradients or spatial patterns in the ChkPt error, often the product of systematic

artefacts and deformation, are particularly evident in the DoD surfaces. Micmac DSMs generated using UAS_{GPS} display erroneous high elevations in the northern end of the site; the topography becomes much more aligned with the Lidar data in the southern end of the site. As noted in previous studies (e.g. James and Robson, 2014; Carbonneau and Dietrich 2017), a central doming effect is present when self-calibration is used. This is of course expected when self-calibration is carried out using only single-scale nadir imagery. The effects of doming seem to be reduced when pre-calibrated parameters are used. The Photoscan DSMs also display erroneous high elevations in the northwest part of the site. Elevation differences are much more prominent along the western margin of the scene when using self-calibration. Even with the use of CtrlPts, self-calibration causes a discrepancy in the northern part of the scene. Camera calibration results differ substantially (Table 2); perhaps the most significant is the focal length estimation. Micmac achieves focal lengths very similar to pre-calibrated values, but Photoscan differs greatly. Correct focal length estimation is known to be one of the most crucial components in a camera calibration model as small errors result in higly exaggerated errors when calculating surface point coordinates through triangulation (Azarbayejani and Pentland, 1995). Camera calibration models usually return the estimation of focal length in relation to pixel size for both pixel width and height. The pixel size of the Sony Exmore R IMX117 used here is known to be 2.4 μm. This was used to also return the estimation of focal length in respect to millimeters. The provided focal length advertised was 8.8 mm.

Table 2. Camera calibration distortion parameters for Photoscan, Micmac and pre-calibration values. Principal point coordinates ($pp\ x, y$) are denoted in pixels with the origin as the top left corner of the camera imaging sensor.

	MatLab	**Photoscan**	**Micmac**

	Pre-calibrated	**dGPS$_{ctrl}$**	**UAS$_{GPS}$**	**dGPS$_{ctrl}$**	**UAS$_{GPS}$**
focal length (pixels)	3.72 x 10^3	3.95 x 10^3	3.66 x 10^3	3.77 x 10^3	3.7 x 10^3
focal length (mm)	8.928	9.480	8.784	9.048	9.048
pp x (pixels)	2.48 x 10^3	2.73 x 10^3	2.77 x 10^3	2.40 x 10^3	2.40 x 10^3
pp y (pixels)	1.82 x 10^3	1.85 x 10^3	1.85 x 10^3	1.82 x 10^3	1.82 x 10^3
k_1 (pixels)	1.94 x 10^{-9}	1.46 x 10^{-9}	1.03 x 10^{-9}	7.63 x 10^{-10}	7.63 x 10^{-10}
k_2 (pixels)	-3.30 x 10^{-16}	-5.13 x 10^{-16}	-3.24 x 10^{-16}	-1.20 x 10^{-16}	-1.20 x 10^{-16}
k_3 (pixels)	1.48 x 10^{-23}	7.35 x 10^{-23}	4.05 x 10^{-23}	8.88 x 10^{-24}	8.88 x 10^{-24}
k_4 (pixels)	-2.78 x 10^{-10}	-1.35 x 10^{-8}	-6.54 x 10^{-9}	-7.63 x 10^{-10}	-7.63 x 10^{-10}
b_1 (pixels)	-1.30 x 10^{-7}	-2.05 x 10^{-3}	-9.27 x 10^{-5}	-8.12 x 10^{-4}	-8.12 x 10^{-4}
b_2 (pixels)	-2.69 x 10^{-11}	-1.76 x 10^{-3}	5.06 x 10^{-4}	-6.41 x 10^{-5}	-6.41 x 10^{-5}
p_1 (pixels)	-3.25 x 10^{-7}	-3.06 x 10^{-7}	-1.09 x 10^{-7}	-2.07 x 10^{-7}	-2.07 x 10^{-7}
p_2 (pixels)	-1.08 x 10^{-6}	-3.39 x 10^{-7}	-1.22 x 10^{-7}	-2.87 x 10^{-7}	-2.87 x 10^{-9}

In respect to RMSE calculations in the elevation axis (between dGPS ChkPts and DSMs), the Micmac reconstruction using the pre-calibrated model and CtrlPts was most accurate (Table 3). Photoscan also achieved its highest accuracy with the CtrlPts-derived pre-calibrated DSM, compared to using UAS$_{GPS}$ and/or self-calibration. No other variables were altered in these comparisons other than camera calibration parameters, which indicates that Micmac's APERO calibration model ('Four') and bundle adjustment routine provide better results than Photoscan's 'Align Photos' tool. The results show that pre-calibration can increase accuracy in Photoscan, although accuracy still does not reach the same quality of Micmac's. DSMs geo-referenced using only UAS$_{GPS}$ data contained larger errors than where CtrlPts were used. This was more prominent in Photoscan reconstructions, suggesting a fundamental difference between Photoscan and Micmac in the handling and weighting of GPS data during the bundle adjustment stage. As expected, larger RMSE on CtrlPts during the bundle adjustment tended

to lead to larger ChkPt RMSE and lower accuracy DSMs. As expected, tie point and camera position RMS also appear to be positively correlated to CtrlPt/ChkPt RMSE values.

Table 3. Control/ChkPt, tie point and camera position statistical results, used to assess the quality of the point cloud and DSMs. All units in meters except where otherwise stated.

	Photoscan				**Micmac**				**Lidar**
	UAS_{GPS}		**$dGPS_{ctrl}$**		**UAS_{GPS}**		**$dGPS_{ctrl}$**		
	Self-Cal	**Pre-Cal**	**Self-Cal**	**Pre-Cal**	**Self-Cal**	**Pre-Cal**	**Self-Cal**	**Pre-Cal**	
CtrlPt RMSE (Z)	2.989	0.604	0.069	0.115	0.783	0.511	0.028	0.030	-
ChkPt RMSE (Z)	1.862	0.506	0.216	0.129	0.518	0.383	0.117	0.113	0.134
ChkPt point Mean Error (Z)	1.879	0.427	0.163	0.114	0.493	0.313	0.106	0.105	-
ChkPt point St.Dev (Z)	0.936	0.335	0.196	0.126	0.429	0.312	0.184	0.179	-
ChkPt point RMSE (X Y)	1.190	0.113	0.243	0.061	0.125	0.170	0.084	0.077	-
ChkPt point Mean Error (X Y)	0.556	0.099	0.236	0.097	0.1055	0.151	0.074	0.070	-
ChkPt point St.Dev (X Y)	0.156	0.058	0.061	0.035	0.069	0.080	0.040	0.034	-
Tie point RMS (pixels)	0.831	0.543	0.722	0.465	0.465	0.387	0.211	0.287	
Camera position RMS	7.850	5.870	6.830	3.603	3.100	2.980	2.765	2.660	

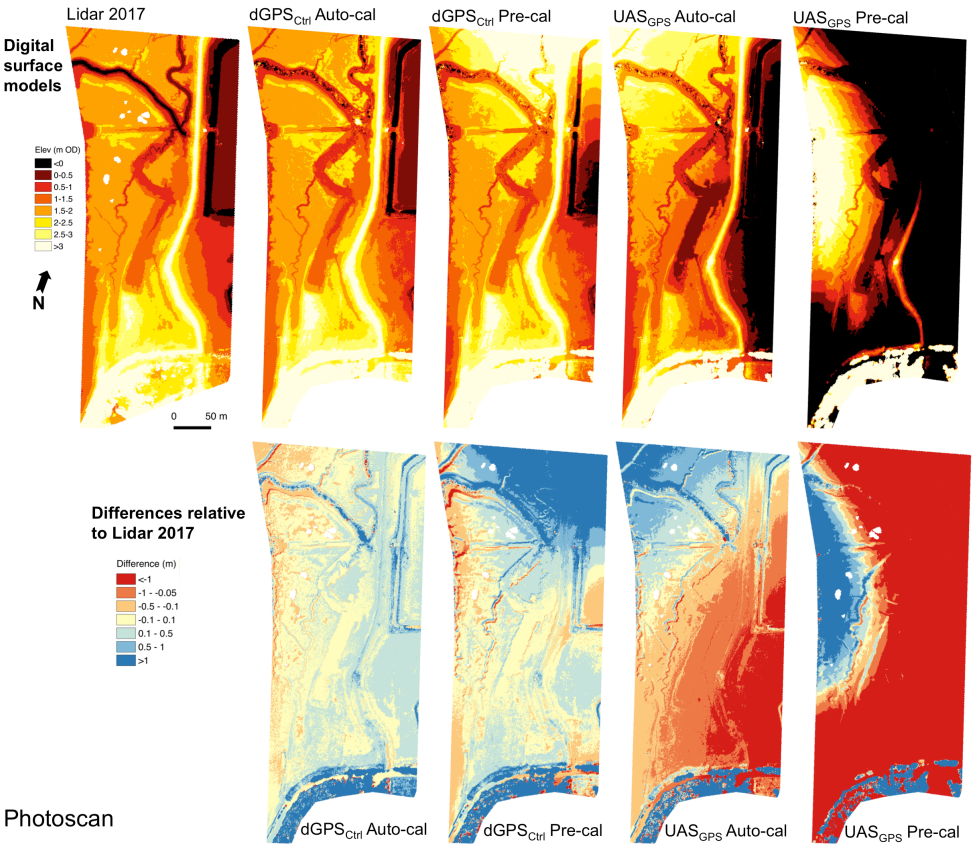

Figure 4. Top: DSMs created using Photoscan and Environment Agency Lidar data. Bottom: DSMs of Difference (DoDs) compared with Lidar data. Strong levels of deformation are clearly visible in reconstructions with poor RMSEs (Table 3). Photoscan produced higher levels deformation in the height (Z) axis than Micmac counterparts.

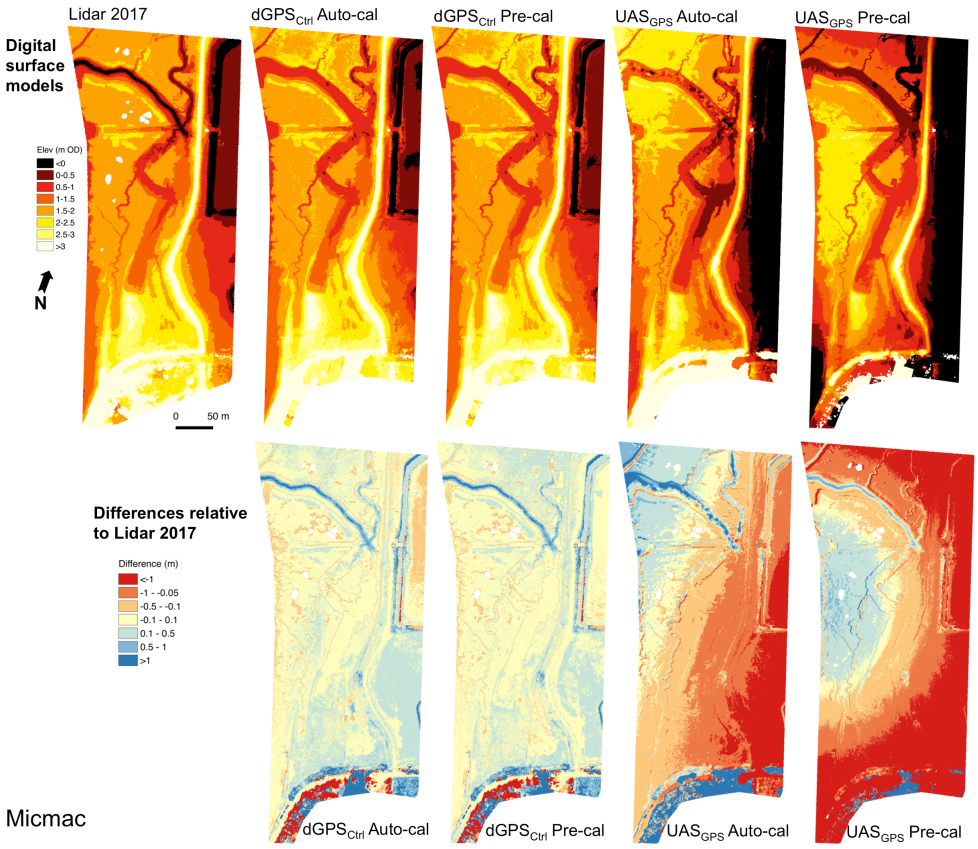

Figure 5. Top: DSMs created using Micmac and Environment Agency Lidar data. Bottom: DSMs of Difference (DoDs) compared with Lidar data. Strong levels of deformation are clearly visible in reconstructions with poor RMSEs (Table 2). The levels of deformation present are significantly lower in Micmac results than Photoscan counterparts.

Transect profiles extracted from the DSMs and Lidar data provide a more distinct representation of the impact of camera calibration on reconstructed topography. In Photoscan the worst results came from the self-calibrated DSM using UAS_{GPS} data (Figure 6A). The effects of pre-calibration clearly reverse the 'doming' effect (although the apparent 'bowling' effect does suggest an overcompensation of distortion parameters). This is represented by the 72% decrease in RMSE-Z from 1.861 m to 0.506 m. This can be compared to the 25% reduction witnessed within Micmac (Figure 6B), which decreased from 0.518 m to 0.383 m. These results demonstrate that Micmac's self-calibration ('Four') distortion model resulted in

more accurate reconstructions in low-amplitude topographies than the Photoscan ('Brown') distortion model. Evidence of the importance of CtrlPts can be observed when comparing UAS_{GPS} with pre-calibration and CtrlPts using self-calibration. In Photoscan, using CtrlPts with self-calibration resulted in a 57% reduction in RMSE than UAS_{GPS} and pre-calibration. This is also similar in Micmac where a 70% reduction was achieved (0.383-0.117 m). Standard deviation of the Z error appears to remain relatively consistent across software packages with the best results obtained for Photoscan and Micmac being 6.05 cm and 7.65 cm respectively.

With respect to errors in the XY plane, it is clear there is a positive correlation with errors in the Z-axis. However, the errors experienced are substantially smaller than the Z-axis counterparts, highlighted by the decreased standard deviation of errors (standard deviation of XY error is on average 20% of Z). This would be expected as systematic surface model deformation from single-scale nadir imagery is more prominent in the Z-axis (as demonstrated by 'doming' and 'bowling').

There is a notable difference in reconstruction of the waterways between Photoscan and Micmac, illustrated at 40 m into the transect (Figure 6). In the Photoscan reconstructions, there are two obvious spikes in elevation, which are not present with the Micmac reconstructions; one of these spikes is present in the Lidar transect (Figure 6). As the surface at this point is water, it likely to be due to deposit of sediment in the waterway. Whilst water surfaces are not expected to be accurately reconstructed using photogrammetric workflows, the results seen here potentially offer valuable information regarding the aggression of depth filtering. Micmac appears to have filtered out the sudden change in elevation as erroneous data points whereas Photoscan is more in line with the Lidar data. Photoscan and Micmac

both offer options for controlling the aggression of depth filtering, however, they are not the same. For each reconstruction, these values were therefore left at their default values. However, the results here suggest that Micmac had much more aggressive depth filtering. As the topography was not very complex this should not have had a significant effect on the final results.

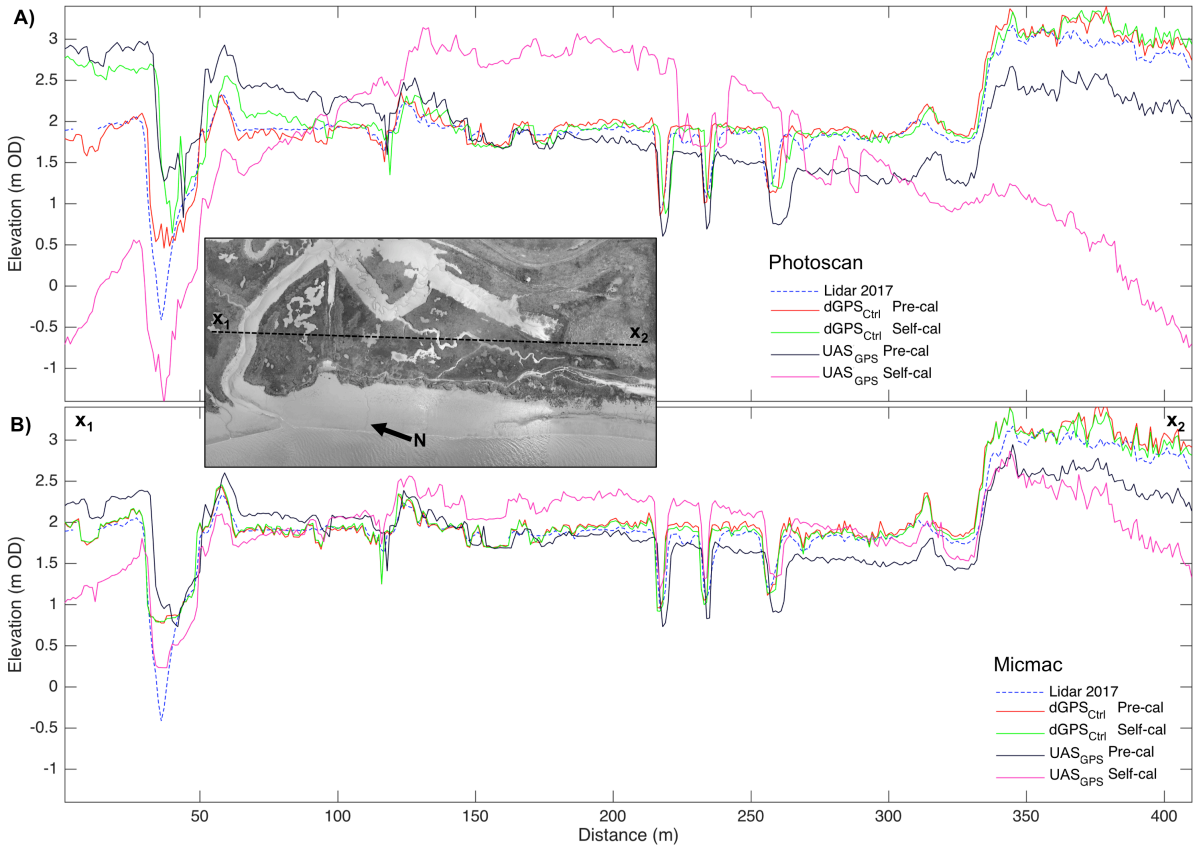

Figure 6 A) Photoscan transect profile extractions. Prior to pre-calibration clear doming can be observed against the 2017 Environment Agency Lidar data. Effective calibration and the use of dGPS can be seen to mitigate such distortion. **B**) Micmac transect profile extractions. A doming effect can be observed when self-calibration is utilised and no CtrlPts are present. The effect is shown to be mitigated with the incorporation of both pre-calibration and CtrlPts.

4. Discussion

The results produced in this paper showcase the possibility for high accuracy UAS 3D surface reconstructions across environments with low topographic variance. The work presented here suggests that when only single-scale nadir imagery is available, pre-calibration of the camera model is more effective at mitigating systematic distortion than self-calibration. This therefore agrees with more photogrammetrically rigorous papers (i.e. James and Robson, 2014; Wackrow and Chandler, 2011; Javernick et al., 2014) although the approach, has been largely overlooked in much of the geoscience literature (e.g. Boon et al., 2016; Casella et al., 2016). The results still depend on accurate pre-calibration, as errors will tend to scale with altitude of the UAS. This caveat has likely led to self-calibration being preferred across much of the literature (Turner et al., 2014). Self-calibration proved more effective at systematic error within Micmac, likely due to the use of the 'Four' distortion model that was designed specifically for aerial imagery. The results obtained from Photoscan suggest that it is not easy to determine accurate parameter values for the Brown distortion model when reconstructing low-amplitude topographies using single-scale nadir imagery. However, this does not indicate that they cannot be suitably defined when convergent imagery is available or when reconstructing a more geometrically diverse topography. The results therefore suggest a full review should to be undertaken into the suitability of common distortion models (i.e. Radial, Brown, Fraser, Four) for a range of real-world topographic contexts. Furthermore, recent literature suggests that over-parameterisation of the camera model can occur in topographies without suitable convergent geometry (such as near-linear topographies) (James et al., 2017b). More applied research into these effects would also be very beneficial to the community.

During self-calibration, the focal length is usually calculated first if it is not already available (Brito, 2017). A poorly estimated focal length would render optimisation of other distortion coefficients (i.e. radial and tangential) incorrect (Rupnik et al., 2017). The results in Table 3 show that in the poorest reconstruction using Photoscan without CtrlPts, the focal length was differed by -1.7% of the pre-calibrated value. This was significantly lower than the estimation using CtrlPts, which differed by 6%. This likely explains the RMSE-Z being lower for the reconstruction using UAS_{GPS} data, and therefore suggests that correct focal length estimation is even more important than CtrlPts when using single-scale nadir only imagery in linear topographies. A lack of robustness is also evident within Photoscan's self-calibration routine. Ideally, camera calibration parameters should not be affected by whether CtrlPts are present. However, this is often only approached when strong converging geometry is available (James and Robson, 2014). In Photoscan it is evident that distortion parameters are being influenced heavily by the inclusion of CtrlPt data in the bundle adjustment. This suggests, as expected, that the low-amplitude topography and single-scale nadir imagery has resulted in poor calibration parameter estimation, which has resulted prominent systematic deformation caused by distortion, when initial parameter values were zero. Alternatively, Photoscan had a smaller number of feature points (192,821) in comparison to Micmac (1,009,906). This could have led to Photoscan being more susceptible to poor sparse point image feature position precision.

When comparing which was more influential on results between the use of CtrlPts or the pre-calibration of the camera, the findings were inconsistent between software. Photoscan suggested pre-calibration was most important whereas Micmac suggested the use of CtrlPts was more significant.. In every case, adding CtrlPts and pre-calibrating improved results and therefore, where possible should be common practise for any UAS survey for 3D surface

reconstruction when using single-scale nadir only imagery. It is well known that dGPS points for both control and ChkPts should be evenly distributed for the most effective use. Furthermore, it is known that a high number of CtrlPts aid the accuracy of reconstructions (Westoby et al., 2012). The ground CtrlPts used in this study were relatively sparse and did not fully cover the whole region due to accessibility issues across the study site. This is likely to be a common issue in geoscience applications as one of the draws of using UASs for surveying is their ability to map environments that would otherwise be a challenge to access with standard surveying equipment. Modern survey-grade UASs benefit from the addition of Real-Time-Kinematic (RTK) GNSS hardware that can achieve cm-level accuracy in positioning. This, in principle, should allow high accuracy results without the need of CtrlPts. This study however, emphasises that the use of CtrlPts alone is not always sufficient to produce high quality reconstructions, and even with top-of-the-range equipment, proper selection and careful parameterisation of a distortion model is essential. Furthermore, real-time corrections (RTK) are not necessary for mapping purposes as all data is post-processed. This perhaps suggests a simple dual-frequency GNSS receiver could be mounted onto a consumer-grade UAS (if not already present), and if post-processing to near-by base station is possible, similar results could be obtained with consumer-grade equipment. These results would likely only improve the horizontal positioning of point clouds as barometers offer more precision for vertical estimates (Bao et al., 2017; Funaki and Hirasawa, 2008). Whilst high stability of the UAS is good for photography purposes, is offers little benefit for a SfM dataset acquisition, with uniform flying being found to increase deformation caused by poorly modelled lens distortion (James and Robson, 2014).

Whilst Agisoft Photoscan and Micmac were selected due to their common practise within the geoscience community, many other packages exist. Although every effort was made to make

the comparison as even as possible, in some instances this was not possible (e.g. sparse point cloud density). This is due to Photoscan not having the same level of customisation as open-source software. The results found here, align with those of Tournadre et al. (2015) and suggest that commercial software solutions without the ability to tailor the reconstruction process specifically to the environment will not produce as accurate results. Micmac also offers a large number of parameters for every function, as well as many different workflow opportunities; therefore, it is sensible to assume there is still lots of untapped potential.

The most important component of the UAS system for creating 3D point clouds is the quality of the camera, and it's pre-calibration. Survey-grade UASs such as senseFly and eBee use (albeit good quality) standard point and shoot cameras. Increased accuracy could be achieved by attaching a high-end Digital Single Lens Reflex (DLSR) camera onto a consumer UAS capable of independent camera fittings (i.e. DJI Inspire 1/2). Moreover, using the 'black-box' commercial software provided with these systems can result in larger than expected (and potentially hidden) errors because results can be easily optained without prior background knowledge in photogrammetry best practices.

5. Conclusion

The findings presented in this paper offer a valuable source of knowledge for UAS 3D mapping of low variance topographies with single-scale nadir imagery. The production of eight DSMs concluded that when using a self-calibrated camera model, broad-scale systematic deformation are present in the form of doming and bowling. Deformation was most pronounced when using UAS_{GPS} data for georeferencing. However, utilising dGPS derived CtrlPts did not fully mitigate distortion. Camera calibration results demonstrated the

importance of choosing a calibration model that could be accurately defined from single-scale nadir-only imagery. In this paper, poor focal length estimations during self-calibration, were shown to cause prominent errors. Various workflow methods were tested, which concluded, in this instance, the incorporation of dGPS CtrlPts and a pre-calibrated camera model can result in systematic distortion being reduced to below detection levels. These findings are significant as they illustrate the importance of correct camera calibration when mapping surfaces of limited topographic variation with single-scale nadir imagery. This further raises the question of whether systematic distortion is reduced or not encountered in more complex topographies, or whether the heterogeneity of such environments simply hides the deformations. Further research in this area would be beneficial to environmental mapping.

Commercial software Photoscan was demonstrated to be a less effective tool for point cloud generation, than the free-to-use open-source Micmac. This was due to a fixed workflow and few self-calibration model options. Micmac demonstrated that the incorporation of a more complex calibration model (Four) can be used to limit deformation of resulting DSM when pre-calibration is not possible. This result suggests that commercial software's do not provide a one-size-fits-all solution and workflows should be adjusted accordingly to topography. Hence, concluding in this instance, knowledge and experience are more valuable assets than expensive software. If dGPS CtrlPts are unavailable, the paper presents a method to correct poor UAS_{GPS} altitude data of consumer-grade UASs using barometer data. The correction significantly improved initial camera pose estimations for the bundle-adjustment, consequently, improving the resulting point cloud. Results demonstrate low-cost UASs and open-source software can be used to generate topographic models that rival aerial Lidar in

accuracy. In this case, producing DSMs with a lower X, Y and Z RMSE, in respect to dGPS derived ChkPts.

6. References

Azarbayejani A and Pentland AP (1995) Recursive estimation of motion, structure, and focal length. *IEEE Transactions on Pattern Analysis and Machine Intelligence* 17(6): 562-575.

Bangen SG, Wheaton JM, Bouwes, N, Bouwes B and Jordan C (2014) A methodological intercomparison of topographic survey techniques for characterizing wadeable streams and rivers. *Geomorphology* 206: 343-361.

Bao X, Xiong Z, Sheng S, Dai Y, Bao S and Liu J (2017) Barometer measurement error modeling and correction for UAH altitude tracking. *Proceedings of Control And Decision Conference*: 3166-3171.

Blewitt G (2016) GPS, Reference Systems. In: Grafarend E (ed) *Encyclopedia of Geodesy*: 1-4.

Bonumá NB, Rossi CG, Arnold JG, Reichert JM, Minella JP, Allen PM and Volk M (2014) Simulating landscape sediment transport capacity by using a modified SWAT model. *Journal of Environmental Quality* 43(1): 55-66.

Boon MA, Greenfield R and Tesfamichael S (2016) Unmanned Aerial Vehicle (UAV) photogrammetry produces accurate high-resolution orthophotos, point clouds and surface models for mapping wetlands. *South African Journal of Geomatics* 5(2): 186-200.

Brasington J, Langham J and Rumsby B (2003) Methodological sensitivity of morphometric estimates of coarse fluvial sediment transport. *Geomorphology*, 53(3): 299-316.

Brito JH (2017) Autocalibration for Structure from Motion. *Computer Vision and Image Understanding* 157: 240-254.

Brown M and Lowe DG (2002) Invariant Features from Interest Point Groups. *Proceedings of the British Machine Vision Conference* 13 (4): 253-262.

Carbonneau PE and Dietrich JT (2017) Cost-effective non-metric photogrammetry from consumer-grade sUAS: implications for direct georeferencing of structure from motion photogrammetry. *Earth Surface Processes and Landforms*, 42(3): 473-486.

Casella E, Rovere A, Pedroncini A, Stark CP, Casella M, Ferrari M and Firpo M (2016) Drones as tools for monitoring beach topography changes in the Ligurian Sea (NW Mediterranean). *Geo-Marine Letters* 36(2): 151-163.

Cea L and French JR (2012) Bathymetric error estimation for the calibration and validation of estuarine hydrodynamic models. *Estuarine, Coastal and Shelf Science* 100: 124-132.

Chandler JH, Shiono K, Rameshwaren P and Lane SN (2001) Measuring flume surfaces for hydraulics research using a Kodak DCS460. *The Photogrammetric Record* 17(97): 39-61.

Chari V and Veeraraghavan A (2014) Lens Distortion, Radial Distortion. In Ikeuchi K (ed) *Computer Vision,* Springer US: 443-445.

Clapuyt F, Vanacker V and Van Oost K (2016) Reproducibility of UAV-based earth topography reconstructions based on Structure-from-Motion algorithms. *Geomorphology* 260: 4-15.

Colomina I and Molina P (2014) Unmanned aerial systems for photogrammetry and remote sensing: A review. *ISPRS Journal of Photogrammetry and Remote Sensing* 92: 79-97.

Environment Agency (2011) Deben Esturay Strategy. Flood Cell 1 Bawdsey Marshes. Available at: http://www.suffolkcoastandheaths.org/estuaries/deben-estuary-partnership/deben-estuary-plan/

Fonstad MA, Dietrich JT, Courville BC, Jensen JL and Carbonneau PE (2013) Topographic structure from motion: a new development in photogrammetric measurement. *Earth Surface Processes and Landforms* 38(4): 421-430.

Fraser CS (2013) Automatic camera calibration in close range photogrammetry. *Photogrammetric Engineering & Remote Sensing* 79(4): 381-388.

Fryer JG and Brown DC (1986) Lens distortion for close-range photogrammetry. *Photogrammetric Engineering and Remote Sensing* 52(1): 51-58.

Funaki M and Hirasawa N (2008) Outline of a small unmanned aerial vehicle (Ant-Plane) designed for Antarctic research. *Polar Science* 2(2): 129-142.

Furukawa Y, Curless B, Seitz SM and Szeliski R (2010) Towards internet-scale multi-view stereo. *Proceedings of IEEE Conference on Computer Vision and Pattern Recognition*: 1434-1441.

Gehrke S, Morin K, Downey M, Boehrer N and Fuchs T (2012) Semi-global matching: An alternative to lidar for DSM generation? *International Archives of the Photogrammetry, Remote Sensing and Spatial Information Sciences*: 38.

Girod L, Nuth C, Kääb A, Etzelmüller B and Kohler J (2017) Terrain changes from images acquired on opportunistic flights by SfM photogrammetry. *The Cryosphere* 11(2): 827-840.

Hirschmuller H (2005) Accurate and efficient stereo processing by semi-global matching and mutual information. *IEEE Conference on Computer Vision and Pattern Recognition (CVPR)* (2): 807–814.

Hutchinson M and Gallant J (2000) Digital elevation models and representation of terrain shape. In Wilson J and Gallant J (ed) *Terrain Analysis: Principles and Applications*, John Wiley & Sons Inc, USA: 29-50.

James MR and Robson S (2012) Straightforward reconstruction of 3D surfaces and topography with a camera: Accuracy and geoscience application. *Journal of Geophysical Research: Earth Science* 117(F03017).

James MR and Robson S (2014) Mitigating systematic error in topographic models derived from UAV and ground-based image networks. *Earth Surface Processes and Landforms* 39(10): 1413-1420.

James MR, Robson S and Smith MW (2017a) 3-D uncertainty-based topographic change detection with structure-from-motion photogrammetry: precision maps for ground control and directly georeferenced surveys. *Earth Surface Processes and Landforms* 42(12): 1769-1788.

James MR, Robson S, d'Oleire-Oltmanns S and Niethammer U (2017b) Optimising UAV topographic surveys processed with structure-from-motion: Ground control quality, quantity and bundle adjustment. *Geomorphology* 280: 51-66.

Javernick L, Brasington J and Caruso B (2014) Modeling the topography of shallow braided rivers using Structure-from-Motion photogrammetry. *Geomorphology* 213: 166-182.

Läbe T and Förstner W (2004) Geometric stability of low-cost digital consumer cameras. *International Archives of the Photogrammetry, Remote Sensing and Spatial Information Sciences* 35(5): 528-535.

Lague D, Brodu N and Leroux J (2013) Accurate 3D comparison of complex topography with terrestrial laser scanner: Application to the Rangitikei canyon (NZ). *ISPRS Journal of Photogrammetry and Remote Sensing* 82: 10-26.

Lowe DG (2004) Distinctive image features from scale-invariant keypoints. *International Journal of Computer Vision* 60(2): 91-110.

Lucieer A, Jong SMD and Turner D (2014) Mapping landslide displacements using Structure from Motion (SfM) and image correlation of multi-temporal UAS photography. *Progress in Physical Geography* 38(1): 97-116.

Luhmann T, Robson S, Kyle S and Boehm J (2013) *Close-Range Photogrammetry and 3D Imaging*. Berlin: Walter de Gruyter, 684pp.

Mancini F, Dubbini M, Gattelli M, Stecchi F, Fabbri S and Gabbianelli G (2013) Using unmanned aerial vehicles (UAV) for high-resolution reconstruction of topography: the structure from motion approach on coastal environments. *Remote Sensing* 5(12): 6880-6898.

Milan DJ, Heritage GL, Large ARG, Fuller IC (2011) Filtering spatial error from DEMs: Implications for morphological change estimation. *Geomorphology* 125: 160-171.

O'Connor J, Smith MJ and James MR (2017) Cameras and settings for aerial surveys in the geosciences: Optimising image data. *Progress in Physical Geography* 41(3): 325-344.

Ouédraogo MM, Degré A, Debouche C and Lisein J (2014) The evaluation of unmanned aerial system-based photogrammetry and terrestrial laser scanning to generate DEMs of agricultural watersheds. *Geomorphology* 214: 339-355.

Pierrot-Deseilligny M and Paparoditis N (2006) A multiresolution and optimization-based image matching approach: An application to surface reconstruction from SPOT5-HRS stereo imagery. *ISPRS Archives - Topographic Mapping from Space (with Special Emphasis on Small Satellites)* 36(1/W41).

Reid C (2013) Possible Causes of Saltmarsh Erosion with Reference to the Deben Estuary, River Deben Association. [online]. Available at: http://www.suffolkcoastandheaths.org/assets/Projects--Partnerships/Saltmarsh-Conf-2015/Possible-Causes-of-saltmarsh-erosion-Carol-Reid-2013.pdf

Rosser N, Dunning SA, Lim M and Petley DN (2005) Terrestrial laser scanning for quantitative rockfall hazard assessment. In Hungr O, Fell R, Couture R and Ebergardt E (eds) *Landslide Risk Management*, Balkema, Amsterdam: 91.

Rupnik E, Daakir M and Deseilligny MP (2017) MicMac-a free, open-source solution for photogrammetry. *Open Geospatial Data, Software and Standards* 2(1): 14.

Smith MW, Carrivick JL and Quincey DJ (2016) Structure from motion photogrammetry in physical geography. *Progress in Physical Geography* 40(2): 247-275

Tang R, Fritsch D and Cramer M (2012) New rigorous and lexible Fourier self-calibration models for airborne camera calibration. *ISPRS Journal of Photogrammetry and Remote Sensing* 71: 76-85.

Tournadre V, Pierrot-Deseilligny M and Faure PH (2015) UAV linear photogrammetry. *International Archives of Photogrammetry, Remote Sensing and Spatial Information Sciences 40*(3): 327.

Triggs B (1998) Autocalibration from planar scenes. *European Conference on Computer Vision* ECCV98: 89-105.

Turner D, Lucieer A and Watson C (2012) An automated technique for generating georectified mosaics from ultra-high resolution unmanned aerial vehicle (UAV) imagery, based on structure from motion (SfM) point clouds. *Remote Sensing* 4(5): 1392-1410.

Wackrow R and Chandler JH (2011) Minimising systematic error surfaces in digital elevation models using oblique convergent imagery. *The Photogrammetric Record* 26(133): 16-31.

Westoby MJ, Brasington J, Glasser NF, Hambrey MJ and Reynolds JM (2012) 'Structure-from-Motion'photogrammetry: A low-cost, effective tool for geoscience applications. *Geomorphology* 179: 300-314.

Wheaton JM, Brasington J, Darby SE and Sear DA (2010) Accounting for uncertainty in DEMs from repeat topographic surveys: improved sediment budgets. *Earth Surface Processes and Landforms* 35(2): 136-156.

Wolf P, DeWitt B, Wilkinson B (2014) *Elements of Photogrammetry with Application in GIS*, McGraw-Hill Education, Maidenhead, 4th edition: 696 pp.

Zhang Z (2000) A flexible new technique for camera calibration. *IEEE Transactions on Pattern Analysis and Machine Intelligence* 22(11): 1330-1334.

7. Appendix

List of commands used for Micmac reconstruction using self-calibration with the use of GPS data and dGPS CtrlPts data respectively. Alteration of the calibration file can be employed to utilise pre-calibration camera parameters.

Command
mm3d OriConvert OriTxtInFile exifdataEven.csv Nav-Brut-RTL ChSys=DegreeWGS84@SysCoRTL.xml MTD=1 CalcV=1
mm3d Tapioca All ".*.JPG" MulScale 400 1500
mm3d Tapas Four15x2 "IM_000[1-9].JPG" DegRadMax=3 DegGen=0 Out=Calib1
mm3d Tapas Four15x2 ".*.JPG" InOri=Calib1 DegGen=2 Out=Calib2
mm3d Tapas AddPolyDeg7 ".*.JPG" InOri=Calib2 Out=Relative
mm3d CenterBascule .*.JPG Relative Nav-Brut-RTL tmp CalcV=1 *
mm3d OriConvert OriTxtInFile exifdataEven.csv Nav-adjusted-RTL
ChSys=DegreeWGS84@SysCoRTL.xml MTD1=1 Delay=0.209629
mm3d CenterBascule .*.JPG Fraser Nav-adjusted-RTL All-RTL
mm3d ChgSysCo .*.JPG All-RTL SysCoRTL.xml@SysCoBL72_EPSG32631.xml All-BL72
mm3d Malt Ortho .*.JPG All-BL72 EZA=1
mm3d Tawny Ortho-MEC-Malt/
mm3d Nuage2Ply MEC-Malt/NuageImProf_STD-MALT_Etape_9.xml Attr=Ortho-MEC-Malt

Command
mm3d Tapioca MulScale ".*.JPG" 400 1500
mm3d Tapas Four15x2 "IMG_000[1-9].JPG" DegRadMax=3 DegGen=0 Out=Calib1
mm3d Tapas Four15x2 ".*.JPG" InOri=Calib1 DegGen=2 Out=Calib2
mm3d Tapas AddPolyDeg7 ".*.JPG" InOri=Calib2 Out=Relative
mm3d GCPBascule ".*.JPG" Relative Georef Dico-Appuis_OS.xml Mesure-Appuis.xml
mm3d Campari ".*.JPG" Georef GeorefCampari GCP=[Dico-Appuis_UTM.xml,1, Mesure-Appuis.xml,1] AllFree=true
mm3d Malt Ortho ".*.JPG" GeorefCampari EZA=1
mm3d Tawny Ortho-MEC-Malt/
mm3d Nuage2Ply MEC-Malt/NuageImProf_STD-MALT_Etape_9.xml Attr=Ortho-MEC-Malt